



HAL
open science

Environmental significance of kaolinite variability over the last centuries in crater lake sediments from Central Mexico

Nathalie Fagel, Isabel Israde-Alcántara, Reza Safaierad, Marttiina Rantala, Sabine Schmidt, Gilles Lepoint, Pierre Pellenard, Nadine Mattielli, Sarah Metcalfe

► To cite this version:

Nathalie Fagel, Isabel Israde-Alcántara, Reza Safaierad, Marttiina Rantala, Sabine Schmidt, et al.. Environmental significance of kaolinite variability over the last centuries in crater lake sediments from Central Mexico. *Applied Clay Science*, 2024, 247, pp.107211. 10.1016/j.clay.2023.107211 . hal-04288213

HAL Id: hal-04288213

<https://hal.science/hal-04288213>

Submitted on 15 Nov 2023

HAL is a multi-disciplinary open access archive for the deposit and dissemination of scientific research documents, whether they are published or not. The documents may come from teaching and research institutions in France or abroad, or from public or private research centers.

L'archive ouverte pluridisciplinaire **HAL**, est destinée au dépôt et à la diffusion de documents scientifiques de niveau recherche, publiés ou non, émanant des établissements d'enseignement et de recherche français ou étrangers, des laboratoires publics ou privés.



Distributed under a Creative Commons Attribution 4.0 International License

1 **Environmental significance of kaolinite variability over the last centuries**
2 **in crater lake sediments from Central Mexico**

3
4 Nathalie Fagel¹, Isabel Israde-Alcantara², Reza Safaierad¹, Marttiina Rantala¹, Sabine
5 Schmidt³, Gilles Lepoint⁴, Pierre Pellenard⁵, Nadine Mattielli⁶ and Sarah Metcalfe⁷

6
7 1. AGEs, Department of Geology, Université de Liège, Belgium, nathalie.fagel@uliege.be.

8 2. Instituto de Investigaciones en Ciencias de la Tierra, Universidad Michoacana de San Nicolás de
9 Hidalgo. Morelia, Michoacán, México

10 3. Univ. Bordeaux, CNRS, Bordeaux INP, EPOC, UMR 5805, F-33600 Pessac, France

11 4. LETIS, Université de Liège, Belgium

12 5. Biogéosciences UMR 6282 CNRS/ub/EPHE, University of Burgundy, Dijon, France

13 6. G-Time, Université Libre de Bruxelles, Belgium

14 7. School of Geography, University of Nottingham, Nottingham NG7 2RD, United Kingdom

15
16
17 **Abstract (239 words)**

18 Environmental conditions have a notable impact on clay minerals, primarily because of the
19 chemical reactions they undergo with their immediate environment. These reactions are
20 more pronounced in hot and humid tropical regions, and therefore, the study of clays
21 deposited at the bottom of lakes in tropical regions can yield valuable insight into past
22 environmental conditions. Here we present multiproxy records, including physical
23 (magnetic susceptibility, grey-scale level and grain size), mineralogical (X-ray diffraction,
24 Simultaneous Thermal Analysis, Fourier-Transform Infrared Spectroscopy), and
25 geochemical (elemental composition by XRF-core scanner, organic geochemistry by IRMS)
26 data, from three ²¹⁰Pb-dated sediment cores (spanning recent centuries < CE 1470) retrieved
27 from crater lakes Los Espinos, Tacámbaro and Teremendo in the Trans-Mexican Volcanic

28 Belt (TMVB), central Mexico. The mineralogical results showed that disordered kaolinite,
29 formed by hydrolysis and hydrothermal alteration, was the predominant mineral in the
30 sediments of the three lakes. The abundance of kaolinite changed in line with organic carbon
31 and organic matter-related elements (Br, S and Ni) and showed opposite trends with
32 lithogenic elements (Ti, K, and Fe). The geochemical data further suggested that increases
33 in kaolinite abundance are linked to the formation of organo-mineral aggregates related to
34 periods of elevated lake productivity that in turn may reflect lake level changes in the closed
35 basins. In Lake Tacámbaro, following the construction of a canal in the early 20th century
36 and subsequent regulation of lake level, the relationship between organic material and
37 kaolinite was no longer present.

38

39 Keywords: XRD Mineralogy; XRF-core scanner; Runoff; Hydrolysis; Tropics; Late
40 Holocene

41

42 **1. Introduction**

43 Central Mexico ([Figure 1](#)) is a suitable area to study climate variability as it lies beyond the
44 northern limit of the Intertropical Convergence Zone (ITCZ) ([Barron et al., 2012](#)), and near the
45 southern limit of the area influenced by the North American Monsoon (NAM) ([Douglas et al.,](#)
46 [1993](#); [Higgins et al., 1999](#)) which, together with convective storms, brings a summer dominated
47 rainfall regime to the area. NAM rainfall is modulated by the El Niño Southern Oscillation
48 (ENSO), with generally reduced/increased summer precipitation during El Niño/La Niña events
49 ([Castro et al., 2001](#)). ENSO is a pseudo-periodic climate pattern involving variations in sea
50 surface temperatures and winds over the eastern tropical Pacific ([McPhaden et al., 2006](#)).

51 The selected study area, i.e. the Trans Mexican Volcanic Belt (TMVB), has widespread
52 crater lakes that are closed systems that may record climatic variability in their sedimentary

53 sequences with relatively limited influence of direct human impact (Alcocer et al., 2000; Cobb
54 et al., 2013). In crater lakes, the lake level is mainly controlled by the water balance between
55 evaporation and precipitation (Gomez-Tagle Chavez et al., 2002). Direct anthropogenic
56 perturbations in the TVMB with an impact on lake water level are recent. In fact, the sharp
57 decrease in the water level of some lakes observed since the 1970s has been explained by the
58 over-exploitation of groundwater for irrigation and urban purposes (Alcocer et al., 2000), which
59 has led to the complete drying of some crater lakes such as La Alberca in 2006 (Kienel et al.,
60 2009) and la Hoya Rincon de Parangueo (Park et al., 2019).

61 In the TMVB area, previous paleolimnological studies have focused on deep (≥ 30 m) and/or
62 large lakes with records of climate variability over the last 30 kyr (La Piscina de Yuriria)
63 (Holmes et al., 2016) to 48 kyr (Pátzacuaro) (Bradbury, 2000). Additionally, only a limited
64 number of laminated sediments with millennial and decadal resolution have been recovered. In
65 Lake Tacámbaro, for example, a Holocene sequence (9.4 kyr BP to 1760 CE) is mainly
66 laminated but the uppermost sediment (~ 190 yr) was lost during coring (Ortega-Guerrero et al.,
67 2021). A centennial to decadal resolved paleoclimatic record for the last 6.7 kyr BP was
68 retrieved from a partly laminated sedimentary sequence from the La Alberca maar lake (Wogau
69 et al., 2019). Short cores from this lake and lake Hoya Rincón de Parangueo, both located in
70 Valle de Santiago, reveal varved sediments for the periods 1852-1973 and 1839-1943 CE,
71 respectively (Kienel et al., 2009). These varved sediments consist of light coloured authigenic
72 carbonate-rich laminae formed by a supersaturated water column during the dry season and
73 dark-coloured detrital laminae formed by surface runoff during the wet season. Although some
74 relationship was observed between detrital sedimentation and local precipitation, it was not
75 significant (Kienel et al., 2009).

76 Lakes are sensitive sensors of environmental and climatic changes (e.g. Adrian et al., 2009),
77 mainly influenced by seasonal temperature and precipitation regimes. In Central Mexico, the

78 increase of temperature starting in spring (Figure 1) favours stable stratification of the upper
79 water column leading to a progressive nutrient limitation in summer, followed by water column
80 mixing in winter (Winder et al., 2009). Such thermal control is manifested, for example, by
81 changes in phytoplankton assemblages in Lake Tacámbaro (Caballero et al., 2016). Rainfall
82 induces surface runoff which carries both organic and mineral detritus into the lake (Kienel et
83 al., 2009). In tropical lakes, spring algal blooms are related to increased temperature, but also
84 nutrients washed into the lake by rainfall (Lind et al., 1992). In summer, the intense rainfall
85 increases water turbidity and dilutes nutrients in the stratified upper water column, leading to a
86 reduction in biological productivity (Gomez-Tagle Chavez et al., 2002). Among other
87 meteorological forcings, the impact of wind action on thermal stratification is limited in crater
88 lakes due to their low surface/depth ratio and steep crater walls (Kienel et al., 2009; Briddon et
89 al., 2023).

90 The mineralogy of crater lake sediments may be used as a reliable proxy for the degree of
91 chemical weathering and physical erosion of the crater soil cover, which in turn reflects the
92 climatic conditions within the closed watershed. Among the detrital minerals, clay minerals
93 are formed in the upper soil profile by the weathering of parent rocks (Pedro, 1968; Singer,
94 1984; Warr, 2022). Their mineralogy reflects the degree of physical decomposition and
95 chemical transformation during pedogenetic processes (Chamley, 1989; Weaver, 1989). Under
96 a warm and humid tropical climate, the intense hydrolysis of primary minerals leads to a
97 complete leaching of cations and partial removal of silica (*i.e.* monosialitisation process). The
98 secondary clay mineral formed, *i.e.* kaolinite $[Al_2Si_2O_5(OH)_4]$, is a combination of a layer of
99 aluminium with a layer of silica (1:1 clay mineral). A stronger hydrolysis leads to a complete
100 leaching of the silica and allows the formation of silica-free secondary phases such as gibbsite
101 $[Al(OH)_3]$, boehmite $[AlO(OH)]$ or diaspore $[AlOOH]$ in association with other immobile
102 elements such as iron (Saalfeld and Wedde, 1974). In addition to climate, the topography and

103 lithology of the parental rock also control clay formation (Singer, 1984). For instance, the
104 volcanic rocks that constitute the parental rock of the crater flanks are more sensitive to
105 weathering than other crystalline rocks. However, according to Chamley (1989), climate
106 remains the most important influencing factor under strongly hydrolysing conditions.

107 The aim of this study is to compare mineralogical and geochemical proxies of three
108 sedimentary cores retrieved from Central Mexico in order to explore the main environmental
109 factors controlling the sedimentary cycle, from alteration processes and erosion to lacustrine
110 sedimentation, over the past centuries. Particular emphasis is given to the evolution and
111 significance of the relative abundance of kaolinite in the sedimentary records.

112

113 **2. Study area**

114 Sediment cores were collected from three crater lakes in the Michoacán-Guanajuato volcanic
115 field, in central part of the TMVB (Figure 1A and 1B). The TMVB is an active volcanic arc,
116 located between $\sim 18^{\circ}30'N$ and $21^{\circ}30'N$, related to the oblique subduction of the Cocos Plate
117 beneath the North American Plate (Ferrari et al., 2012). The studied lakes in the TMVB
118 constitute promising sites for high-resolution paleolimnological studies (Figure 1C). These
119 lakes correspond to “maars” that originated by phreatomagmatic eruptions (Cifuentes and
120 Fucugauchi, 1999) and range in altitude from 1475 to 2058 masl.

121 Based on meteorological data (30-year average: 1981-2010) from three stations near the
122 lakes (Figure 1D), the mean monthly temperature in Tacámbaro ranges from 17 to 22°C (annual
123 average 19°C) while the temperatures are slightly cooler in Teremendo ($14 \leq T \leq 20^{\circ}C$) and
124 Villa Jimenez (i.e. the station located 2 km NE of Lake Los Espinos, $13 \leq T \leq 21^{\circ}C$). More than
125 92% of the annual precipitation falls in summer, from late May to October (Figure 1B).
126 Tacámbaro is characterized by the highest mean annual precipitation of 1168 mm/yr.

127 Teremendo is the driest location with 700 mm/yr, whereas Villa Jimenez station displays
128 intermediate values with 896 mm/yr.

129 [Insert Figure 1]

130 Los Espinos crater (19°54'25" N, 101°46'06" W, 1940 masl - [Figure 1C](#)) is a well-preserved
131 tuff volcanic cone located on the north-western margin of the Zacapu tectonic lacustrine basin
132 ([Hasenaka and Carmichael, 1985](#)). Its formation dates back to 25 kyr BP. Its basement consists
133 of basalts and andesites, which are hosted in granitic rocks ([Sigala et al., 2017](#)). The crater has
134 an elliptical shape (0.33 km²) with a NE-SW orientation and accommodates a lake of 350 m in
135 diameter (area 0.1 km²) with a maximum depth of 30 m ([Siebe et al., 2012](#)). The water column
136 is mixed in winter (December-February) but stratified during the rest of the year ([Hernández-
137 Morales et al., 2011](#)). The chlorophyll a ranges between 0.5 and 1.5 mg/m³. The inner slopes
138 of the crater are vegetated with tropical deciduous and gallery forests, helping to reduce the
139 movement of sediments downslope into the lake.

140 The Tacámbaro crater (19°12'38" N, 101°27'33" W, 1475 masl - [Figure 1C](#)) was formed
141 during the Pliocene ([Guilbaud et al., 2012](#)). Its volcanic basement is made of basalts and dacites
142 whereas the youngest < 1 Ma volcanic rocks are andesite and basaltic andesites ([Guilbaud et
143 al., 2012](#)). In this location, the host rocks are made of siliciclastic and carbonate rocks ([Sigala
144 et al., 2017](#)). The crater is characterized by steep walls (28 m) and narrow shore zones, except
145 on its eastern flank ([Ortega-Guerrero et al., 2021](#)). The lake is small with a diameter of 300 m
146 (surface area 0.08 km²) and a maximum depth of 28 m ([Caballero et al., 2016; Sigala et al.,
147 2017](#)). The lake was a closed system until the construction of a canal at the beginning of the
148 20th century to regulate the lake depth ([Ortega-Guerrero et al., 2021](#)). The lake type is warm
149 monomictic, yearly stratified except in January ([Hernández-Morales, 2011](#)). It is characterized
150 by eutrophic conditions with annual maximum chlorophyll a concentrations ranging from 25 to

151 75 mg/m³ (Sigala et al., 2017). The vegetation of the crater is diverse, ranging from a typical
152 temperate forest to a low deciduous forest (Morales et al., 2008).

153 The Teremendo crater (0.65 km²), formed during the Pliocene, has steep walls made of
154 basalts and andesites overlying granitic basement (Soria-Caballero et al., 2019). The crater lake
155 (19°48'25" N, 101°27'15" W, 2058 masl - Figure 1C) is shallow (depth ≤ 9 m) (Sigala et al.,
156 2017) and covers an area of 0.15 km² with a circular shape. The lake stratifies from March to
157 November and is hypertrophic with an annual chlorophyll a concentration of ≥ 75 mg/m³
158 (Sigala et al., 2017). Based on field observations, the crater is covered by a seasonal dry forest,
159 which has been partially deforested and replaced by cattle pasture and shrubland. Additionally,
160 the marginal areas of the lake are colonized by (semi-)aquatic plants.

161

162 **3. Material and methods**

163 3.1. Sedimentological analyses

164 In June 2019, three crater lakes in Central Mexico were sampled using a Uwitec® gravity
165 corer, with a 9 cm core barrel. Cores were retrieved in the central part of each lake, namely
166 LLEs19-2 (53 cm, water depth 30 m) from Lake Los Espinos, LTa19-3 (93.5 cm, water depth
167 26 m) from Lake Tacámbaro and LTe19-4 (109 cm, water depth 8 m) from Lake Teremendo
168 (Figure 1B & 1C). After the fieldtrip, the three cores were split lengthwise, described and
169 photographed. Before transport, one half-core section was subsampled in one or two contiguous
170 4 cm wide rectangular plastic tubes ≤ 74 cm long for non-destructive analyses and into 25 cm
171 long x 4 cm wide x 1.5 cm deep aluminium boxes for destructive analyses. The second half-
172 core section was stored at 4°C for diatom and pollen analyses.

173 The subsamples within the plastic channels were scanned for physical (grayscale image,
174 magnetic susceptibility) and X-ray Fluorescence (XRF) geochemical characterization of the
175 sediment. Magnetic susceptibility (MS) of the sediment was measured at 5 mm intervals using

176 a Bartington® instrument MS2E point sensor, following the protocol described in [Bartington-](#)
177 [Instruments \(2008\)](#). Three measurements expressed in SI units, equivalent to 10^{-6} CGS, were
178 averaged to obtain a representative profile (AGEs, Belgium). A SCOPIX X-ray image-
179 processing system (EPOC, University of Bordeaux, France) was used at 58 kV, 10 mA and a
180 step size of 15 μm to determine the grayscale image of the sediment cores ([Migeon et al., 1998](#)).

181 Wet bulk density was calculated by weighing 1 cm^3 of wet sediment at 1 cm intervals for the
182 top 25 cm of the cores. Grain-size analyses were done with a sampling resolution of 4 to 5 cm
183 using a Malvern® Mastersizer 2000 laser diffraction particle analyser (ARGENCO, University
184 of Liège, Belgium). Each bulk sediment sample was dispersed in deionised water, sieved to 2
185 mm and introduced into the dispersion unit cell (Hydro 2000G). The sample volume was
186 adjusted to reach a laser beam obscuration of $10\pm 5\%$. Before analysis, the sample was
187 homogenised using a 2000 rpm stirrer and disaggregated using moderate ultrasonic waves (i.e.
188 2.6 W power). An average of three measurements was calculated for data reproducibility. The
189 relative abundance of clay (i.e. $< 2 \mu\text{m}$), silt (2-63 μm) and sand ($> 63 \mu\text{m}$) fractions was
190 calculated for each sample. The silt fraction was subdivided into fine (2-10 μm), medium (10-
191 30 μm) and coarse silt (30-63 μm) fractions.

192 Mineralogical analysis was performed by X-ray diffraction (XRD) using a Bruker® D8-
193 Advance Eco diffractometer (CuK α radiance, $\lambda=1.5418\text{\AA}$, 40 KV, 25 mA) coupled with a
194 Lynxeye XE detector (AGEs, University of Liège). The sampling resolution reaches up to 1 cm
195 for LTA19-3 (n=72) and 4 to 5 cm for LLEs19-3 (n=10) and LTe19-4 (n=22). The dried (40°C)
196 bulk sediment sample was ground by hand with an agate mortar. The powder was sieved at $<$
197 150 μm and transferred to a plastic holder using the backside method ([Moore and Reynolds,](#)
198 [1989](#)) and scanned from 2 to 70° 2 θ with a step size of 0.009°2 θ and 0.5 seconds per step.
199 Mineral identification and quantification were done using the EVA and TOPAS ® Bruker

200 software, respectively. A Rietveld refinement was applied to all the minerals identified by XRD
201 ([Rietveld, 1967](#); [Brindley, 1980b](#); [Bish, 1993a](#); [Środoń, 2002](#)). Preferred orientations and unit
202 cell parameters of the mineral phases were progressively adjusted to obtain a reconstructed
203 XRD pattern as close as possible to the measured pattern.

204 To complement the XRD analysis, a Simultaneous Thermal Analyser (STA, Mettler-
205 Toledo® STAR^e System) was used to follow the origin and transformation processes of the
206 clay minerals through the sedimentary cycle. STA allows the degree of order-disorder of
207 individual clay minerals to be estimated, giving clues on their origin and transformation
208 processes (e.g. [Patterson and Swaffield, 1987](#); [Hemminger and Cammenga, 1989](#); [Emmerich,](#)
209 [2010](#)). Thermal analysis also provides information on the presence of disordered ([Smykatz,](#)
210 [1974](#); [Drits et al., 1995](#)) and/or amorphous mineral phases, even at low abundances ([Emmerich,](#)
211 [2010](#)). The presence of these phases, which remain largely undetected in the XRD analysis, is
212 indicative of mineral transformation and/or dissolution occurring in specific environmental
213 conditions (e.g. pedogenesis, weathering). STA analysis was made on bulk sediment powder
214 on a selection of 12 samples from the 3 cores characterized by variable proportions of kaolinite
215 (AGEs, University of Liège). The sample weight loss (Thermogravimetric TG curve) and
216 associated heat exchanges (Differential Scanning Calorimetry DSC curve) were followed at a
217 constant heating rate of 20°C per minute from 25 to 1200°C under a nitrogen atmosphere (80
218 ml/min). The first derivative of the thermogravimetric curve (DTG) represents the rate of
219 weight loss. It was calculated since DTG peak gives the specific temperatures characteristic of
220 the different mineral components more accurately than the TG curve and indicates the
221 characteristic temperature of the reactions occurring in the samples ([Földvári, 2011](#)), in
222 particular dehydration and dehydroxylation for clay minerals. The STA data were processed
223 using the evaluation software Metler Toledo STAR^e SW16.40.

224 Fourier Transform Infrared Spectroscopy (FTIR) was carried out on 8 samples already

225 analyzed by STA using a Nicolet NEXUS Spectrometer (Laboratory of Mineralogy, University
226 of Liège). Pellets were made from 2 mg of powdered sample, ground to $< 250 \mu\text{m}$ and 148 mg
227 of potassium bromide. The measurement was made in the range of 4000 to 400 cm^{-1} with a
228 resolution of 1 cm^{-1} . FTIR is a method commonly used to assess the degree of disorder (Lorentz
229 et al., 2018).

230 Scanning Electron Microscope (SEM) imaging was carried out at the University of
231 Burgundy (ARCEN analytical platform) on 6 samples using a Hitachi SU8230, with a
232 resolution of 0.8 nm (15kV, WD = 4 mm), equipped with a ThermoFisher Scientific UltraDry
233 30 mm² Energy Dispersive X-ray (EDS, 127 eV Mn energetic resolution) in order to comfort
234 XRD and geochemical analyses. Sieved sediments at $30 \mu\text{m}$ were used for observations after
235 aqueous suspension of the sediment on a SEM spinner covered with copper tape and
236 hydrophilization under air plasma in primary vacuum.

237 An Avaatech XRF core scanner (EPOC, University of Bordeaux, France) equipped with a
238 Fe-Mo tube was used with a step size of 1 mm to characterize the bulk sediment geochemistry
239 (e.g. Frugone-Álvarez et al., 2017). Measurements of fourteen elements (i.e. Al, Si, S, K, Ca,
240 Ti, Mn, Fe, Co, Ni, Br, Sr, Zr and Pb) were done with voltages of 10, 30 and 50 kV and counting
241 times of 15, 20 and 25 seconds, respectively. Semi-quantitative concentration profiles of the
242 elements were plotted through the depth of the sediment core based on the variation of their
243 peak areas measured on XRF spectra and expressed as counts per second (cps). A statistical
244 approach was applied to the XRF dataset using version 4.2.2 of the R environment (R
245 Development Core Team, 2013). First, the XRF count data were transformed to centred log-
246 ratio (clr) using *rgr* package (Garrett and Garrett, 2018). A Robust Principal Component
247 Analysis (RPCA, Candès et al., 2011) was then applied to the clr data using the package *pcaPP*
248 (Filzmoser et al., 2018) as proposed by Żarczyński et al. (2019). The 14 elements were included
249 in the analysis. The principal components (PC) with an eigenvalue > 1 were retained as

250 significant for the total variance of the dataset (Davis, 2002).

251 Sediment organic geochemistry, including organic carbon (C) and nitrogen (N) stable
252 isotope ratios ($\delta^{13}\text{C}$, $\delta^{15}\text{N}$) and elemental concentrations, was characterized by Isotope Ratio
253 Mass Spectrometry (IRMS)/Elemental Analyzer (EA) at LETIS (University of Liège,
254 Belgium). The analysis was carried out at ~4 to 10 cm intervals using a VarioMicro Elementar
255 analyser coupled to a precisiON IRMS (LTe19-4). Prior to the analysis, the samples were
256 acidified by exposing the freeze-dried and ground sediments to 37% HCl vapor for 10 hours to
257 remove carbonates. Bulk N was considered to comprise primarily organic nitrogen given the
258 generally low concentration of inorganic nitrogen in lake sediments. For LTe19-4, the analysis
259 was additionally carried out on non-acidified samples to evaluate the influence of acidification
260 on elemental concentrations and isotope ratios. The patterns of acidified and non-acidified
261 samples were consistent for all four variables ($R^2 > 0.94$) indicating that the trends are reliable.
262 All values used in this study for the three lakes are from acidified samples. Variations in carbon
263 and nitrogen isotope ratios are expressed using the delta-notation, i.e., as differences (‰)
264 relative to international standards (VPDB for carbon, AIR for nitrogen). Precision of the $\delta^{13}\text{C}$
265 and $\delta^{15}\text{N}$ measurements based on repeat analyses were ± 0.27 and 0.97 SD, respectively. The
266 carbon to nitrogen ratio (C/N) was calculated for each sample to estimate changes in the relative
267 contribution of allochthonous and autochthonous organic matter (Meyers, 2003). C/N mass
268 ratios were converted into atomic ratios by multiplying the values by 1.167.

269 3.2. Core chronology

270 The activities of ^{210}Pb , ^{226}Ra and ^{232}Th were measured on 1 cm thick samples in cores
271 LLEs19-2, LTa19-3 and LTe19-4 with a low-background and high-efficiency well-type gamma
272 detector (EPOC, University of Bordeaux, France) until negligible excess ^{210}Pb was reached.
273 The excess ^{210}Pb activities ($^{210}\text{Pb}_{\text{xs}}$) were calculated by subtracting the measured ^{226}Ra content
274 from the total ^{210}Pb content. The Constant Flux/Constant Sedimentation model (CF/CS,

275 [Appleby and Oldfield, 1978](#)) was applied to the $^{210}\text{Pb}_{\text{xs}}$ to calculate a mean sediment
276 accumulation rate, which was used to estimate an age for each sediment layer.

277

278 **4. Results**

279 4.1. Sedimentology

280 [Figure 2](#) presents the SCOPIX image of the cores LLEs19-2 (Espinosa), LLa19-3
281 (Tacámbaro) and LTe19-4 (Teremendo), along with the MS profiles and the abundance of clay
282 ($\% < 2 \mu\text{m}$) and fine silt ($\% 2\text{-}10 \mu\text{m}$) fractions ([Table S1](#)).

283 [\[Insert Figure 2\]](#)

284 The sediment of LLEs19-2 was brownish dark (5YR 2/1, [Munsell, 1975](#)) with a fine organic-
285 rich texture (average 24 % organic matter), dominated by silt ($78\pm 5\%$) and sand ($20\pm 5\%$) with
286 a small proportion of clay ($2.6\pm 0.9\%$). Its MS profile ranged between $2.96 \cdot 10^{-4}$ and $6.30 \cdot 10^{-3}$ SI,
287 with an average value of $1.55 \cdot 10^{-3}$ SI. The MS displayed a few positive excursions between 10
288 and 15 cm, 33 to 35 cm and 49-51 cm, underlying darker and coarser multi-millimeter
289 laminations. The highest sand fraction (29%) corresponded to the darker laminations at 14-15
290 cm. In the upper part of the SCOPIX image, a vertical burrow disturbed several mm-scale
291 laminations observed between 4 and 7 cm. The lower part of the core (from 35 to 53 cm) was
292 marked by abundant gastropod shells, especially between 35 and 43 cm.

293 The background colour of sediment core LLa19-3 was dusky brown (5YR 2/2) with several
294 darker (brownish black 5 YR 2/2) multi-millimeter laminations ([Munsell, 1975](#)). A few shells
295 were observed, especially in the lower core section (73-93.5 cm). The core was mainly
296 composed of silt particles ($80\pm 7\%$) associated with $20\pm 7\%$ sand. The core section comprised
297 between 39 and 52 cm was characterized by higher proportions of both clay (10 to 15%) and
298 fine silt fractions (35 to 45%) than the core average (i.e. $5.5\pm 3\%$ and $26\pm 8\%$, respectively). The

299 LTA19-3 core displayed a similar range of MS variation from $3.48 \cdot 10^{-4}$ to 6.310^{-3} SI as in the
300 LLEs19-2 core but with a higher average value ($2.03 \cdot 10^{-3}$ SI). The MS values were low ($0.8 \cdot 10^{-3}$
301 SI) in the lower part of the core, increased up to 60 cm and then decreased irregularly from
302 ~52 cm upwards. The organic matter content of the LTA19-3 core was on average 20% and
303 reached up to 25% in the lower core section (60-93.5 cm).

304 The sediment in core LTe19-4 was brownish dark (5YR 2/1, [Munsell, 1975](#)) with a fine
305 organic-rich texture (average 23% organic matter). The sediment was composed of silt ($77 \pm 8\%$)
306 and sand grains ($23 \pm 8\%$) with a low proportion of clay particles ($3.4 \pm 1\%$). The sediment texture
307 comprised mm-scale darker laminations between 95 and 49 cm and was more homogeneous in
308 the upper 49 cm. The MS profile of core LTe19-4 ranged from $2.37 \cdot 10^{-4}$ to $2.51 \cdot 10^{-3}$ SI. The
309 MS displayed a minimum value between 103.5 and 100 cm, in an interval containing the highest
310 sandy fraction of the core (45% at 100-101 cm). MS fluctuated between 93.5 and 49 with 4
311 distinct peaks, also visible in the SCOPIX image, at 93.5, 61, 54.5 and 49.5 cm, followed by a
312 decline from 49 cm upwards.

313 4.2. Mineralogy

314 Andesite (i.e. plagioclase) and kaolinite were the two main minerals identified in the three
315 studied sediment cores, associated with diopside (i.e. pyroxene), hornblende (i.e. amphibole)
316 and/or forsterite (i.e. olivine) and quartz ([Table S2](#)). Carbonate minerals, ubiquitous in LLEs19-
317 2 (except at 14-15 cm) and in LTe19-4, were represented by calcite, aragonite and/or dolomite.
318 In contrast, carbonate minerals were absent from Tacámbaro. In addition, accessory minerals
319 such as oxides (i.e. hematite, magnetite) or sulphide (pyrite) were detected in some samples.
320 The diffraction band observed between 20 and 30° 2θ revealed the presence of amorphous
321 sedimentary components such as biogenic silica, organic matter or volcanic glass (e.g. [Fagel et](#)
322 [al., 2017](#)).

323 In LLEs19-2 ([Table S2a](#)), andesite (plagioclase) was the most abundant mineral (43% \pm 12)
324 followed by kaolinite (33% \pm 8). The secondary phases were pyroxene (i.e. diopside, 7% \pm 2.3)
325 and carbonates, with both calcite (6.6% \pm 4.5) and aragonite (4.6% \pm 2.8). Quartz was present in
326 trace amounts (1-3%) in all samples. Forsterite (2-6%) and hornblende (1-2%) were present in
327 trace amounts. In addition to kaolinite, the phyllosilicates were also represented by traces of
328 talc (\leq 1%), observed in a few samples.

329 With a core mean of 58% \pm 8, the relative abundance of kaolinite in LTA19-3 was higher than
330 in LLEs19-2 with a range of variation between 37 and 76%. Traces of diaspore (0-2%) were
331 suspected in the upper 60 cm core section whereas its abundance was slightly higher in the
332 lower core section (3-6% - [Table S2b](#)). Andesite was the second most abundant mineral (24%
333 \pm 5) in LTA19-3. Cristobalite represented an average abundance of 10% \pm 3. Hornblende (< 3%)
334 and diopside (< 1%) were present in low abundance in most samples. Quartz and hematite were
335 ubiquitous whereas magnetite was identified in trace amounts (\leq 2%) in some samples. Traces
336 of forsterite or talc were observed in only one sample. To get an overview of the mineral
337 composition in LTA19-3 some XRD patterns are reported by core depth in [Figure S1](#). With the
338 exception of talc and hornblende, which were found in only one sample, most minerals were
339 detected in all samples, but at variable intensities quantified by Topas. As an example, [Figure](#)
340 [S2](#) compares the raw XRD spectra of sample LTA19-3 15-16 cm with the Topas-derived
341 reconstructed profile. For kaolinite, in particular, the unit cell parameters were modified from
342 the structure given by [Bish \(1993b\)](#). A Rietveld refinement was first obtained by imposing two
343 planes of preferential orientation (i.e. 001 and 100) and then by adjusting the unit cell
344 parameters (a, b, c, α , β and γ). The cif file obtained is reported in the supplementary material
345 ([Text S1a](#)).

346 Kaolinite (52% \pm 6) was the dominant mineral observed in LTe19-4, ranging from 41% at
347 54-55 cm to 65% at 100-101 cm. Kaolinite was followed by andesite (38% \pm 4). The other

348 magmatic minerals (i.e. diopside, forsterite and hornblende) were only observed in one or two
349 samples (Table S2c). Traces of cristobalite (< 2%) were only detected in the upper samples (0-
350 11 cm). Calcite (3.7% ±2) was present in low abundance in all samples, except in the uppermost
351 (0-1 cm). Quartz (2.7% ±0.7) was ubiquitous. Dolomite and hematite were detected in traces in
352 most samples.

353 In the three sedimentary cores, kaolinite was the unique clay mineral evidenced by a large
354 reflection at 7.3Å in the bulk mineralogy of all samples (Figure S1), confirmed by SEM
355 observation (Figure S3). The TG curves displayed at least 2 main peaks between 50-130 °C and
356 400-500 °C corresponding to 5-7% and 8-12% of mass loss, respectively (Figure 3). The DTG
357 curves specified the temperature of these endothermic reactions, i.e. 73-98 °C and 444-474 °C
358 respectively. A third exothermic peak was observed at 890-990°C associated with a mass loss
359 of ~3-5%. After heating up to 1200 °C the total weight loss averaged 20-33% of the original
360 sample weight.

361 [Insert Figure 3]

362 The FTIR analyses were done on two or three samples per core, those samples being
363 characterized by a range of abundance in kaolinite (i.e. 27 to 41% in LLEs19-2; 59 to 76% in
364 LTa19-3; 50 to 59% in LTe19-4). The samples from Tacámbaro and Teremendo displayed
365 similar FTIR spectra with two absorption bands in the 3690-3620 cm⁻¹ region and several bands
366 over 1000 and 500 cm⁻¹. Note the first two adsorption bands near 3700-3600 cm⁻¹ were not
367 detected in the two samples from LLEs19-2 that were characterized by the lowest abundance
368 of kaolinite in the bulk sediment.

369 [Insert Figure 4]

370 4.3. Sediment geochemistry

371 XRF element profiles, SCOPIX curves, clay abundance and organic geochemistry of the
372 three cores are plotted against core depth in Figure 5. For LLEs19-2, Ti covaried inversely with

373 the SCOPIX greyscale level (Figure 5) whereas Br mimicked the SCOPIX curve. The darker
374 sediment layers characterized by low SCOPIX levels corresponded to positive incursions in Ti
375 but negative incursions in Br. Sediment organic carbon (C) and nitrogen (N) contents in
376 LLEs19-2 followed a pattern similar to that of Br that may be associated with organic matter in
377 lake sediments (Ziegler et al., 2008; Davies et al., 2015). The relative abundance of clay (< 2
378 μm fraction) followed a reverse pattern. Similarly, an opposite pattern was observed for $\delta^{13}\text{C}$
379 that displayed the lowest (most ^{13}C -depleted) values during periods of elevated organic content
380 and Br. C/N ratio and $\delta^{15}\text{N}$ in LLEs19-2 showed a gradual declining trend towards the sediment
381 surface and, overall, a relatively small range of variability.

382 [Insert Figure 5]

383 In LTA19-3, XRF elements and SCOPIX values showed similar coeval variation as in
384 LLEs19-2 (Figure 5). For example, a marked decrease in Ti counts observed between 58 and
385 62 cm corresponded to an increase in Br and SCOPIX values. Similarly, sediment C and N
386 covaried with Br, and decreasing $\delta^{13}\text{C}$ values were generally associated with increasing organic
387 content and Br. Clay (< 2 μm fraction) abundance showed little variability in the lower part of
388 the record (up to around 60 cm) whereon it followed a pattern somewhat similar to Ti. C/N
389 values showed a gradual decline in the lower part of the core (~90-65 cm), with a distinct peak
390 (> 25) at around 60 cm. Sediment $\delta^{15}\text{N}$ values showed few trends aside from a step increase at
391 around 60 cm.

392 For LTe19-4, Ti depicted an inverse trend with SCOPIX values and Br (Figure 5), consistent
393 with LLEs19-2 and LTA19-3. Compared to the other two lakes, the variations in LTe19-4 were
394 generally more stable aside from a pronounced decrease in Ti in the lower part of the core,
395 between ~104 and 94 cm, and a corresponding increase in Br. Sediment C and N data are not
396 available for this section of the core but both indicators reflect higher organic content between
397 ~90 and 75 cm, consistent with slightly elevated Br. An increasing trend in C and N, and to a

398 lesser extent in Br, was also observed in the upper 20 cm of the core. As in LLEs19-2, clay (<
399 2 μm fraction) abundance followed a pattern reverse to those observed in Br, C and N. Sediment
400 $\delta^{13}\text{C}$ and C/N displayed distinctly low and high values, respectively, in the lower part of the
401 core (i.e. ~ 75 cm downward), however, their variation was less clearly linked to variations in
402 the XRF elements.

403 Regarding the RPCA, the first two PCs in core LLEs19-2 were sufficient to explain a
404 cumulated variance of 74% (PC1 63%, PC2 11%). In the PC1-PC2 biplot diagram (Figure S4),
405 the elements were clustered into two main groups aligned along the PC1 axis (see the
406 correlation matrix given in Figure S4). Ti, Fe, Zr, Co, Sr and K (group 1) were aligned along
407 the positive PC1 axis. Ni, Br and S associated with Si and Al (group 2) plotted along the
408 negative PC1 axis. Ca varied along the positive PC2 axis. Pb and Mn were the less significant
409 elements in the distribution, located in an intermediate position between PC1 and PC2.

410 In core LTa19-3, the elements were distributed in 3 groups and 69% of the variance was
411 explained by 3 PCs (i.e. PC1 45%, PC2 14%, PC3 10%). The first two groups were aligned
412 along the PC1 axis whereas group 3 was associated with the PC2 axis. Group 1 (Ti, Fe, Co, Zr,
413 Mn and Pb but with a low contribution data in Figure S4) was associated with negative PC1
414 axis values whereas group 2 (S and Br associated with Ni and Al) was distributed along the
415 positive PC1 axis. Group 3 (Ca, Sr and K) was clustered along the PC2 axis.

416 The RPCA analysis on LTe19-4 revealed 4 significant PCs (i.e. PC1 31%, PC2 21%, PC3
417 15%, PC4 13%) with a cumulative variance of 80%. The elements were scattered in the PC1-
418 PC2 binary plot. At least 4 groups of elements were evidenced, i.e., Ni, Sr and Br (group 1),
419 Co, Fe and Zr (group 2), Ti, Si and K (group 3) and, Pb and Ca (group 4) whereas Al and Sr
420 were not significant (correlation matrix given in Figure S4).

421

422 4.4. Core chronology

423 In LLEs19-2, the $^{210}\text{Pb}_{\text{xs}}$ activity decreased from 288 mBq/g at 2.5 cm down to a negligible
424 level at 16.5 cm, giving a low sediment accumulation rate of 0.09 cm/yr. For LTA19-3, the
425 relatively constant $^{210}\text{Pb}_{\text{xs}}$ activity in the upper 5 cm suggested a mixed layer, which is
426 consistent with the homogeneous texture underlined by the SCOPIX image (Figure 2). Below
427 this mixed layer, the decrease in ^{210}Pb excesses resulted in a sediment accumulation rate of 0.6
428 cm/yr. LTe19-4 presented a rather regular exponential decrease of $^{210}\text{Pb}_{\text{xs}}$ reaching negligible
429 activities at about 25 cm, resulting in an intermediate sediment accumulation rate of 0.255 cm/yr
430 compared to the other two lakes.

431 The age models of the three cores (Figure S5) were derived from the depth profiles of $^{210}\text{Pb}_{\text{xs}}$
432 in the upper 17, 23 and 61 cm of the sediment in cores LLEs19-2, LTe19-4 and LTA19-3,
433 respectively. Assuming a surface age of AD2019 (i.e. coring year) and a constant sediment
434 accumulation rate, LTA19-3 covers an interval of less than 160 yr whereas LLEs19-2 and
435 LTe19-4 are well beyond the timescale of $^{210}\text{Pb}_{\text{xs}}$ with ~430 yr in LTe19-4 and ≤ 600 yr in
436 LLEs19-2. In terms of temporal resolution, only the sedimentation rate for LTA19-3 would
437 allow a sufficient resolution to investigate pluriannual ENSO variability with a sampling
438 resolution of 1 cm (i.e. 1 cm corresponds to 1.7 years for LTA19-3, 4 years for LTe19-4 and 11
439 years for LLEs19-2).

440

441 **5. Discussion**

442 5.1. Origin of minerals

443 In the three studied crater lakes, the mineralogical assemblages are composed of variable
444 proportions of primary minerals, probably derived from the volcanic crater substrate by
445 erosion and runoff and secondary minerals formed by weathering and pedogenetic processes
446 in the upper soil cover and possibly by hydrothermal alteration. The volcanic-derived

447 primary minerals are dominated by andesite (up to 54% in LLEs19-2), which may be
448 associated with some forsterite, diopside and/or amphibole (Table S2).

449 Concerning the clay minerals, the origin of kaolinite is most probably multifold. First,
450 kaolinite is a ubiquitous secondary mineral, whose abundance reaches 65% in LTe19-4 and
451 up to 74% in LTa19-3, whereas it accounts for less than 45% in LLEs19-2 (Table S2). SEM
452 observations (Figure S3) confirmed that, at least, part of the kaolinite was formed by
453 weathering of primary magmatic-derived plagioclase or Fe-Mg minerals. The presence of
454 secondary kaolinite in the sediments of the three studied lakes probably reflects moderate
455 hydrolysis conditions under tropical warm and humid conditions in the soils (e.g. Chamley,
456 1989) covering the internal crater flanks. Crater lakes represent small and closed sedimentary
457 basins with a rapid source-to-sink transfer. Clay minerals in their sediments are useful
458 indicators of paleoclimate conditions. However, pedogenesis is a slow process and the
459 abundance of kaolinite observed in the crater lake sediments most likely reflects weathering
460 conditions over the past millennia (Thiry, 2000).

461 Second, the broad reflection at 7.3 Å observed in the bulk XRD patterns of the Mexican
462 lacustrine samples may indicate the presence of some halloysite-7 Å in addition to kaolinite.
463 Halloysite-10 Å, renamed hydrohalloysite (Hatert et al., 2023), has been found in weathered or
464 hydrothermally altered rocks, saprolites, and soils (Joussein et al., 2005). Hydrohalloysite is
465 especially abundant in newly formed volcanic ash soils associated with quartz and cristobalite,
466 formed by hydrothermal alteration of volcanic rocks at low temperatures (e.g., in New Zealand,
467 Joussein et al., 2005). Such an origin is consistent with the volcanic substrate of the lakes
468 studied and the presence of cristobalite. Sample preparation may explain the absence of
469 hydrohalloysite in the crater lake samples, as hydrohalloysite can be quickly transformed into
470 halloysite-7 Å under ambient temperature and humidity conditions or by heating $\geq 40^\circ\text{C}$
471 (Joussein et al., 2005). In addition, hydrohalloysite has been considered as an early weathering

472 product in lateritic soils (Robert and Herbillon, 1990), representing an intermediate weathering
473 stage between recent soil rich in allophane and more weathered soils rich in kaolinite and iron
474 oxides in tropical and subtropical areas (Ndayiragije and Delvaux, 2004). The abundance of
475 halloysite relative to kaolinite would decrease with increasing weathering stage (Joussein et al.,
476 2005).

477 In Tacámbaro, the association of kaolinite with some diaspore, confirmed by SEM
478 observation (Figure S3), indicates complete leaching of silica under strong hydrolysis
479 corresponding to an alitisation process. This process is indicative of stronger drainage that
480 may occur along the steepest slope of the crater flank. The presence of both kaolinite and
481 diaspore only in LTa19-3 emphasizes stronger chemical weathering conditions in the Lake
482 Tacámbaro catchment.

483 Among the other minerals observed, the presence of carbonates in all samples of LLEs19-
484 2, except in the dark layer at 14-15 cm (Figure 2), reflects a biological component mainly
485 associated with gastropod shells. In LTe19-4, some carbonates are detected by XRD. These
486 carbonates are probably authigenic and related to the productivity of the lake as there are no
487 carbonates in the watershed. Cristobalite is most probably related to the presence of volcanic
488 glass. In addition, the abundance of cristobalite, especially in LTa19-3 ($\leq 16\%$), could reflect
489 the diatom productivity of the water column, as opal is an unstable amorphous silica mineral.
490 The transition from amorphous opal-A to crystallised opal-CT (CT for cristobalite-tridymite)
491 is a continuum controlled by a microscale dissolution-reprecipitation process in a near-surface
492 environment (Jones and Renaut, 2007). Opal-A is progressively converted to opal-CT due to a
493 decrease in d-spacing and porosity and an associated increase in density (Rice et al., 1995).
494 Jones and Renaut (2007) emphasized that this process can be accelerated by the addition of Si
495 from external sources. Indeed, such supply is supported in closed tropical crater lakes by silica-
496 rich leachate solution delivered by monosialitisation and eventually alitisation processes.

497

498 5.2. Characterisation of 1:1 layer

499 In the bulk powder XRD patterns the broad reflection at 7.3 Å reflects the presence of a
500 poorly ordered kaolinite, most probably in association with some halloysite-7 Å. Halloysite-7
501 Å is characterized by a broad reflection at 7.3 Å, which is difficult to decipher with a poorly
502 ordered kaolinite, particularly when they are mixed (Brindley, 1980a). A few percentages of
503 hydrohalloysite (cif file obtained reported on Text S1b) were found, in addition to kaolinite, in
504 the bulk and clay < 2 µm fraction of at least one surface soil of the crater lake Teremendo
505 (Figure S6). In the following text, the term kaolinite is used *sensu lato* for a mixture of kaolinite
506 and some halloysite-7 Å.

507 The thermogram (TG) curves display two main mass losses characteristic of kaolinitic clays
508 (Figure 4). The first endothermic mass loss at 40-130°C corresponds to the loss of adsorbed
509 water. This pronounced endothermic reaction is consistent with the presence of both disordered
510 kaolinite and halloysite-7 Å (Emmerich, 2010).

511 The second pronounced endothermic peak corresponds to the dehydroxylation of
512 kaolinite/halloysite and its transformation in metakaolinite (e.g. Wang et al., 2011). The
513 temperature of the reaction, as measured by DTG curves, is between 444 and 474°C, whereas
514 the dehydroxylation of kaolinite often occurs at higher temperatures between 530 and 630°C
515 (Emmerich, 2010). However, the measured dehydroxylation temperature is influenced by
516 several factors, such as the mineral assemblage and, in particular, the abundance of kaolinite in
517 the sample (Anand and Gilkes, 1987), the crystallinity of kaolinite (Földvári, 2011) but also the
518 experimental conditions (Guggenheim and Van Groos, 2001; Heide and Földvári, 2006). Anand
519 and Gilkes (1987) observed an increase in dehydroxylation temperature from 454 to 491°C with
520 increasing kaolinite abundance in soil samples. According to Földvári (2011), the position of
521 the dehydroxylation peak was observed in lower temperature ranges for disordered kaolinites

522 (530-570°C) than for ordered kaolinites (570-630°C). For the studied samples, there is no clear
523 relationship between the abundance of kaolinite in the bulk sample (i.e. between 27 and 76%)
524 and the dihydroxylation temperature. Therefore, the kaolinites studied most probably
525 correspond to extremely disordered crystals (Smykatz, 1974), associated with some halloysite-
526 7 Å.

527 A third mass loss of 3 to 5% occurring between 890 and 990°C corresponds to a small
528 exothermic peak associated with the crystallisation of mullite ($\text{Al}_2\text{Si}_2\text{O}_7$). Again, the observed
529 lower temperature range for this reaction (usually 940-1000°C) and the moderate heat exchange
530 confirm the disordered character of kaolinite (Emmerich, 2010) and the presence of some
531 halloysite-7 Å.

532 FTIR spectra (Figure 4) confirms the poorly crystallized character of kaolinite. Well-ordered
533 kaolinite is characterized by four absorption bands in the 3700-3600 cm^{-1} range associated with
534 the stretching of OH-groups and by two absorption bands in the 1000-900 cm^{-1} range associated
535 with the bending (Bich et al., 2009). However, the FTIR spectra from Tacámbaro and
536 Teremendo samples display only two absorption bands between 3700 and 3620 cm^{-1} (i.e. at
537 3689-3699 and 3618-3622 cm^{-1} - Figure 4). The absence of vibration bands at 3670 and 3650
538 cm^{-1} indicates poorly order kaolinite (Vaculikova et al., 2011). It is also supported by the
539 presence of only one absorption band identified in the 1000-900 cm^{-1} range (i.e. between 908
540 and 916 cm^{-1}) due to the OH deformation of inner hydroxyl group (Vaculikova et al., 2011).
541 Note the peak near 540 cm^{-1} that coincides with Al-O-Si deformation in kaolinite (Madejová et
542 al., 2010)

543 In addition to kaolinite, a mass loss (~5%) observed in the TG curve (Figure 3) between the
544 dehydration and dehydroxylation reactions reflects the presence of organic matter
545 (Mackenzie, 1957) and hydrated phases such as opal in the bulk sediment. In the FTIR spectra
546 (Figure 4), the absorption bands at 794-796 and 467-474 cm^{-1} confirmed the presence of silica

547 minerals (i.e., quartz and cristobalite in XRD patterns). Related to the Si-O-Si bending
548 vibration, they usually grow from crystalline to non-crystalline varieties like opal A (Graetsch,
549 1994). The absence of absorption bands between 3090 and 3460 cm^{-1} confirms the absence of
550 gibbsite and boehmite (Kloprogge et al., 2002), which were not detected by XRD. Note that the
551 presence of diaspore, evidenced by SEM in LTa19-3 (Figure S3), was not confirmed by FTIR
552 (Frost et al., 1999).

553

554 5.3. Significance of kaolinite variability in the sedimentary record

555 Figure 5 shows the parallel evolution of kaolinite in regard to the Br/Ti ratio, i.e. a ratio
556 selected as a proxy for lake productivity (Agnihotri et al., 2008). The use of Br/Ti as a reliable
557 proxy for lake productivity in the studied lakes is supported by the bulk organic matter
558 geochemistry (Figure 5). In all three lakes, the concomitant increases in sediment organic
559 content (C and N) and Br/Ti were matched by generally low or declining $\delta^{13}\text{C}$ values, likely
560 related to increased phytoplankton productivity (Meyers, 2003). Similar low $\delta^{13}\text{C}$ values may
561 also be associated with terrestrial organic matter from C3 plants (typical values around -27%)
562 (Meyers, 1997), however, the opposite patterns for detrital elements (such as Ti) provide no
563 evidence for increased catchment material fluxes. C/N values, often used to indicate relative
564 changes in autochthonous and allochthonous organic matter inputs, showed few consistent
565 changes but the generally low values point to a strong autochthonous component (Meyers,
566 2003) suggesting that the shifts in sediment C and N content (and thus Br/Ti) are tightly
567 connected to primary production in the lake.

568 In LLEs19-2, the kaolinite abundance, which varies by a factor of 2 over the last 5 centuries
569 follows a parallel trend with the Br/Ti ratio (Figure 6). The highest kaolinite abundance ϕ (i.e.
570 45% at 23-24 cm) corresponds to a high Br/Ti ratio. The LLEs19-2 record displays four distinct
571 intervals with higher kaolinite abundance: ca. 1450, 1600, 1760-1820 and 1940-1980 CE.

572 [Insert Figure 6]

573 In LTe19-4, the kaolinite abundance ranges from 41 to 65% over the last four centuries, with
574 three intervals marked by higher kaolinite abundance at ~1640-1740, 1830-1900 and 1950-
575 2019 CE. Although the range of variation is smaller than in LLEs19-2, the maximum abundance
576 of kaolinite (i.e. 65% at 100-101 cm) also coincides with a pronounced positive excursion in
577 the Br/Ti ratio around ca. 1650 CE. An increase in kaolinite is observed in the LLEs19-2 record
578 within a similar time window (~1600 CE).

579 Due to a higher sedimentation rate, the core LTa19-3 covers only 160 years, allowing a high
580 temporal resolution. In this short time period, the kaolinite profile (Figure 6) displays a broad
581 variation (37-74%) with higher values observed in two intervals, i.e. in the lower part of the
582 record (1865-1875 CE) and between 1930-1985 CE. As in core LLEs19-2, and to some extent
583 in LTe19-4, the kaolinite abundance follows the evolution of the Br/Ti ratio in the lower part
584 of the record (93-55 cm, ~1860-1925 CE). It is hypothesized that the covariance between
585 kaolinite abundance and the Br/Ti ratios reflects lake productivity and, by extension, natural
586 variations in lake level. In spring, warmer temperatures favour high biological productivity and
587 keep lake level low through evaporation. The onset of rainfall brings nutrients and detrital
588 material, including kaolinite-rich clayey particles, into the lake. The sedimentation of kaolinite
589 may then be related to its rapid adsorption on the abundant organic matter present in the water
590 column (Guo et al., 2023) and to the settling of the organo-mineral aggregates due to their
591 density. This is supported by the low abundance of clay-sized particles during organic-rich
592 periods, particularly distinct in LLEs19-2 (Figure 5).

593 There is no obvious relationship between the regional (Harris et al., 2020) or local
594 temperature data (CONAGUA-SMN web platform, <http://clicom-mex.cicese.mx>) and the
595 kaolinite profile in core LTa19-3. The lowest temperature interval recorded in the local
596 meteorological data (1950-1990 CE) does not coincide with the lowest kaolinite abundance in

597 LTA19-3. The sharp increase in kaolinite observed during 1925-1930 CE occurs during an
598 interval of low regional temperatures but it is consistent with an increase in local precipitation.

599 In the upper section of core LTA19-3, there is no clear relationship between the Br/Ti ratio
600 and kaolinite (Figure 6). The kaolinite abundance varies rather in parallel with Ti, although the
601 different resolution of the two proxies prevents a detailed comparison. This sharp change
602 probably reflects a local disturbance around Lake Tacámbaro. [Ortega-Guerrero et al. \(2021\)](#)
603 reported that the water level of Lake Tacámbaro was regulated by the construction of an
604 artificial canal in the early 20th century. The exact date of this human intervention is unknown.
605 The distinct peak in C/N values at around 60 cm ([Figure 5](#)), coincident with the decoupling
606 between kaolinite and Br/Ti ratio ([Figure 6](#)), may well indicate a transient increase in catchment
607 inputs associated with the construction work. After the construction of the canal, the sharp
608 increase in kaolinite occurs during an interval of increased local rainfall. This change in local
609 meteorological conditions (i.e. the sharpest change during the 20th century) probably enhances
610 surface runoff, delivering more detrital elements and kaolinite to Lake Tacámbaro.

611

612 **Conclusions**

613 • Disordered kaolinite is the dominant secondary mineral present in all sediment samples
614 from the 3 crater lakes investigated. This clay mineral is partly formed by moderate hydrolysis,
615 a process consistent with the regional tropical warm and humid conditions of Central Mexico.

616 • The broad reflection at 7.3 Å observed in the bulk XRD patterns of the Mexican
617 lacustrine samples underlines the presence of some halloysite-7 Å in addition to kaolinite.
618 Halloysite is most probably formed by hydrothermal alteration of volcanic glasses.

619 • The presence of diaspore in Lake Tacámbaro probably reflects a more efficient local
620 drainage along the steepest slope of the crater, resulting in complete removal of silica.

621 • Statistical treatment of the XRF core scanner data indicates an opposite relationship
622 between detrital elements (Ti, K, Fe) and organic matter-related elements (Br, S, Ni).

623 • In lakes Los Espinos and Teremendo, the kaolinite abundance is the highest when the
624 detrital flux (e.g. Ti) is the lowest and the organic matter flux is the highest. Kaolinite may be
625 adsorbed onto the organic matter particles present in the water column and then settle to the
626 lake bottom. Under natural conditions, the kaolinite abundance in the crater lake sediments may
627 be a proxy for lake productivity and an indirect proxy for lake level (i.e. higher kaolinite
628 abundance associated with lower lake level).

629 • For Lake Tacámbaro, the construction of a canal in the early 20th century to regulate the
630 lake level suppresses the link between the kaolinite and lake productivity observed in the lower
631 core section (pre-1925 CE). In the upper core section (i.e. post 1925 CE), kaolinite covaries
632 with detrital elements such as Ti which are carried by surface runoff. The abundance of kaolinite
633 is sensitive to rainfall intensity particularly when human intervention regulates lake levels.

634

635 **Acknowledgments**

636

637 The fieldwork was done in June 2019 by N. Fagel and I. Israde-Alcantara, with the help of
638 Luis Matilde Gacia, Julio Cañas, David Sanchez and Angel Zamudio. Thanks to Arturo Chacon
639 for providing a boat location. Part of the analysis costs was supported by a FNRS funding for
640 the PDR proposal HolMecl 2020-2025. The authors thank Joel Otten and Nicolas Delmelle
641 (Geology, ULiège) for their technical support with the sedimentological and mineralogical
642 preparations and analyses. Subsampling and sedimentological analyses were done as part of the
643 master thesis of Gaelle Wanlin. Prof. Frédéric Boulvain (Sedimentology, ULiège) brought his
644 expertise on sedimentological features and core description. Prof. Frédéric Hatert (Mineralogy,
645 ULiège) helped with the TOPAS software. SEM-EDS observations were made with the support
646 of Régis Parvaud, ARCEM analytical platform of the University of Burgundy (Dijon, France).

647 **References**

- 648 Adrian, R., O'Reilly, C.M., Zagarese, H., Baines, S.B., Hessen, D.O., Keller, W., Livingstone, D.M., Sommaruga,
649 R., Straile, D., Van Donk, E., 2009. Lakes as sentinels of climate change. *Limnology and oceanography*
650 54, 2283-2297.
- 651 Agnihotri, R., Altabet, M.A., Herbert, T.D., Tierney, J.E., 2008. Subdecadally resolved paleoceanography of the
652 Peru margin during the last two millennia. *Geochemistry, Geophysics, Geosystems* 9.
- 653 Alcocer, J., Escobar, E., Lugo, A., 2000. Water use (and abuse) and its effects on the crater-lakes of Valle de
654 Santiago, Mexico. *Lakes & Reservoirs: Research & Management* 5, 145-149.
- 655 Anand, R., Gilkes, R., 1987. An application of thermogravimetry to quantitative studies of feldspar alteration in
656 soils. *Journal of Thermal Analysis and Calorimetry* 32, 1163-1175.
- 657 Appleby, P.G., Oldfield, F., 1978. The calculation of lead-210 dates assuming a constant rate of supply of
658 unsupported ²¹⁰Pb to the sediment. *Catena* 5, 1-8.
- 659 Barron, J.A., Metcalfe, S.E., Addison, J.A., 2012. Response of the North American monsoon to regional changes
660 in ocean surface temperature. *Paleoceanography* 27.
- 661 Bartington-Instruments, 2008. OM0408 - Operation manual for MS2 magnetic susceptibility system. Bartington
662 Instruments Limited. Oxford, England.
- 663 Bich, C., Ambroise, J., Péra, J., 2009. Influence of degree of dehydroxylation on the pozzolanic activity of
664 metakaolin. *Applied Clay Science* 44, 194-200.
- 665 Bish, D.L., 1993a. Rietveld refinement of the kaolinite structure at 1.5 K. *Clays and Clay Minerals* 41, 738-744.
- 666 Bish, D.L., 1993b. Studies of clays and clay minerals using X-ray powder diffraction and the Rietveld method.
667 Los Alamos National Lab., NM (United States).
- 668 Bradbury, J.P., 2000. Limnologic history of Lago de Patzcuaro, Michoacan, Mexico for the past 48,000 years:
669 impacts of climate and man. *Palaeogeography, Palaeoclimatology, Palaeoecology* 163, 69-95.
- 670 Briddon, C.L., Metcalfe, S., Taylor, D., Bannister, W., Cunanan, M., Santos-Borja, A.C., Papa, R.D., McGowan,
671 S., 2023. Changing water quality and thermocline depth along an aquaculture gradient in six tropical
672 crater lakes. *Hydrobiologia* 850, 283-299.
- 673 Brindley, G.W., 1980a. Order-disorder in the clay mineral structures, in: Brindley, G.W., Brown, G. (Eds.), *Crystal*
674 *Structures of Clay Minerals and their X-ray Identification*. Mineralogical Society, London, pp. 125-196.
- 675 Brindley, G.W., 1980b. Quantative analysis of clay mixtures, in: Brindley, G.W., Brown, G. (Eds.), *Crystal*
676 *Structures of Clay Minerals and their X-ray Identification*. Mineralogical Society, London, pp. 125-196.

677 Caballero, M., Vázquez, G., Ortega, B., Favila, M.E., Lozano-García, S., 2016. Responses to a warming trend and
678 “El Niño” events in a tropical lake in western México. *Aquatic Sciences* 78, 591-604.

679 Candès, E.J., Li, X., Ma, Y., Wright, J., 2011. Robust principal component analysis? *Journal of Association for*
680 *computing machinery* 57, 1-37.

681 Castro, C.L., McKee, T.B., Pielke, R.A., 2001. The relationship of the North American monsoon to tropical and
682 North Pacific sea surface temperatures as revealed by observational analyses. *Journal of Climate* 14,
683 4449-4473.

684 Chamley, H., 1989. Clay formation through weathering. *Clay sedimentology*, 21-50.

685 Cifuentes, R.M.U., Fucugauchi, J.U., 1999. Paleomagnetic study of the Valle de Santiago volcanics, Michoacán-
686 Guanajuato volcanic field, Mexico. *Geofísica Internacional* 38, 217-230.

687 Cobb, K.M., Westphal, N., Sayani, H.R., Watson, J.T., Di Lorenzo, E., Cheng, H., Edwards, R., Charles, C.D.,
688 2013. Highly variable El Niño–southern oscillation throughout the Holocene. *Science* 339, 67-70.

689 Davies, S.J., Lamb, H.F., Roberts, S.J., 2015. Micro-XRF core scanning in palaeolimnology: recent developments.
690 Micro-XRF studies of sediment cores: Applications of a non-destructive tool for the environmental
691 sciences, 189-226.

692 Davis, J.C., 2002. *Statistics and data analysis in Geology*. Wiley & sons, New York.

693 Douglas, M.W., Maddox, R.A., Howard, K., Reyes, S., 1993. The mexican monsoon. *Journal of Climate* 6, 1665-
694 1677.

695 Drits, V., Besson, G., Muller, F., 1995. An improved model for structural transformations of heat-treated
696 aluminous dioctahedral 2: 1 layer silicates. *Clays and Clay minerals* 43, 718-731.

697 Emmerich, K., 2010. *Thermal analysis in the characterization and processing of industrial minerals*.

698 Fagel, N., Alvarez, D., Namur, O., Devidal, J.-L., Nuttin, L., Schmidt, S., Jana, P., Torrejon, F., Bertrand, S.,
699 Araneda, A., 2017. Lacustrine record of last millennia eruptions in Northern Chilean Patagonia (45–47°
700 S). *The Holocene* 27, 1227-1251.

701 Ferrari, L., Orozco-Esquivel, T., Manea, V., Manea, M., 2012. The dynamic history of the Trans-Mexican
702 Volcanic Belt and the Mexico subduction zone. *Tectonophysics* 522, 122-149.

703 Filzmoser, P., Fritz, H., Kalcher, K., 2018. *pcaPP: Robust PCA by Projection Pursuit*. R Foundation for Statistical
704 Computing, Vienna, Austria.

705 Földvári, M., 2011. *Handbook of thermogravimetric system of minerals and its use in geological practice*.
706 Geological Institute of Hungary Budapest.

707 Frost, R.L., Klopogge, J.T., Russell, S.C., Szetu, J., 1999. Dehydroxylation and the vibrational spectroscopy of
708 aluminum (oxo) hydroxides using infrared emission spectroscopy. Part III: diaspore. *Applied*
709 *Spectroscopy* 53, 829-835.

710 Frugone-Álvarez, M., Latorre, C., Giralt, S., Polanco-Martínez, J., Bernárdez, P., Oliva-Urcia, B., Maldonado, A.,
711 Carrevedo, M.L., Moreno, A., Delgado Huertas, A., 2017. A 7000-year high-resolution lake sediment
712 record from coastal central Chile (Lago Vichuquén, 34° S): implications for past sea level and
713 environmental variability. *Journal of Quaternary Science* 32, 830-844.

714 Garrett, R.G., Garrett, M.R.G., 2018. Package 'rgr'. *Appl Geochemistry EDA*.

715 Gomez-Tagle Chavez, A., Bernal-Brooks, F., Alcocer, J., 2002. Sensitivity of Mexican water bodies to regional
716 climatic change: three study alternatives applied to remote sensed data of Lake Patzcuaro. *Hydrobiologia*
717 467, 169-176.

718 Graetsch, H., 1994. Structural characteristics of opaline and microcrystalline silica minerals. *Reviews in*
719 *Mineralogy and Geochemistry* 29, 209-232.

720 Guggenheim, S., Van Groos, A.K., 2001. Baseline studies of the clay minerals society source clays: thermal
721 analysis. *Clays and Clay Minerals* 49, 433-443.

722 Guilbaud, M.-N., Siebe, C., Layer, P., Salinas, S., 2012. Reconstruction of the volcanic history of the Tacámbaro-
723 Puruarán area (Michoacán, México) reveals high frequency of Holocene monogenetic eruptions. *Bulletin*
724 *of volcanology* 74, 1187-1211.

725 Guo, C., Guo, L., Bass, S., Manning, A.J., Jin, Z., Zhou, Y., 2023. On the role of organic matter composition in
726 fresh-water kaolinite flocculation. *Journal of Environmental Management* 345, 118576.

727 Harris, I., Osborn, T.J., Jones, P., Lister, D., 2020. Version 4 of the CRU TS monthly high-resolution gridded
728 multivariate climate dataset. *Scientific data* 7, 109.

729 Hasenaka, T., Carmichael, I.S.E., 1985. The cinder cones of Michoacan-Guanajuato, central Mexico: their age,
730 volume and distribution, and magma discharge rate. *Journal of Volcanology and Geothermal Research*
731 25, 105-124.

732 Hatert, F., Mills, S.J., Pasero, M., Miyawaki, R., Bosi, F., 2023. CNMNC guidelines for the nomenclature of
733 polymorphs and polysomes. *Mineralogical Magazine* 87, 225-232.

734 Heide, K., Földvari, M., 2006. High temperature mass spectrometric gas-release studies of kaolinite Al₂ [Si₂O₅
735 (OH) ₄] decomposition. *Thermochimica Acta* 446, 106-112.

736 Hemminger, W.F., Cammenga, H.K., 1989. *Methoden des thermischen analyse*. Springer Verlag, Heidelberg,
737 Germany.

738 Hernández-Morales, R., 2011. Fitoplancton de los lagos cráter de Michoacán, México.

739 Hernández-Morales, R., Ortega, M., Sánchez, J., Alvarado, R., Aguilera, M., 2011. Distribución estacional del
740 fitoplancton en un lago cálido monomíctico en Michoacán, México. *Biológicas Revista de la DES*
741 *Ciencias Biológico Agropecuarias Universidad Michoacana de San Nicolás de Hidalgo* 13, 21-28.

742 Higgins, R.W., Chen, Y., Douglas, A.V., 1999. Interannual variability of the North American warm season
743 precipitation regime. *Journal of Climate* 12, 653-680.

744 Holmes, J.A., Metcalfe, S.E., Jones, H.L., Marshall, J.D., 2016. Climatic variability over the last 30 000 years
745 recorded in La Piscina de Yuriria, a Central Mexican crater lake. *Journal of Quaternary science* 31, 310-
746 324.

747 Jones, B., Renaut, R.W., 2007. Microstructural changes accompanying the opal-A to opal-CT transition: New
748 evidence from the siliceous sinters of Geysir, Haukadalur, Iceland. *Sedimentology* 54, 921-948.

749 Joussein, E., Petit, S., Churchman, J., Theng, B., Righi, D., Delvaux, B., 2005. Halloysite clay minerals—a review.
750 *Clay minerals* 40, 383-426.

751 Kienel, U., Bowen, S.W., Byrne, R., Park, J., Böhnelt, H., Dulski, P., Luhr, J.F., Siebert, L., Haug, G.H.,
752 Negendank, J.F., 2009. First lacustrine varve chronologies from Mexico: impact of droughts, ENSO and
753 human activity since AD 1840 as recorded in maar sediments from Valle de Santiago. *Journal of*
754 *Paleolimnology* 42, 587-609.

755 Klopogge, J.T., Ruan, H.D., Frost, R.L., 2002. Thermal decomposition of bauxite minerals: infrared emission
756 spectroscopy of gibbsite, boehmite and diaspor. *Journal of materials science* 37, 1121-1129.

757 Lind, O.T., Doyle, R., Vodopich, D.S., Trotter, B.G., Limón, J.G., Dcivalos-Lind, L., 1992. Clay turbidity:
758 Regulation of phytoplankton production in a large, nutrient-rich tropical lake. *Limnology and*
759 *Oceanography* 37, 549-565.

760 Lorentz, B., Shanahan, N., Stetsko, Y.P., Zayed, A., 2018. Characterization of Florida kaolin clays using multiple-
761 technique approach. *Applied Clay Science* 161, 326-333.

762 Mackenzie, R.C., 1957. *The differential thermal investigation of clays*.

763 Madejová, J., Balan, E., Petit, S., 2010. Application of vibrational spectroscopy to the characterization of
764 phyllosilicates and other industrial minerals.

765 McPhaden, M.J., Zebiak, S.E., Glantz, M.H., 2006. ENSO as an integrating concept in earth science. *science* 314,
766 1740-1745.

767 Meyers, P.A., 1997. Organic geochemical proxies of paleoceanographic, paleolimnologic, and paleoclimatic
768 processes. *Organic geochemistry* 27, 213-250.

769 Meyers, P.A., 2003. Applications of organic geochemistry to paleolimnological reconstructions: a summary of
770 examples from the Laurentian Great Lakes. *Organic geochemistry* 34, 261-289.

771 Migeon, S., Weber, O., Faugeres, J.-C., Saint-Paul, J., 1998. SCOPIX: a new X-ray imaging system for core
772 analysis. *Geo-Marine Letters* 18, 251-255.

773 Moore, D.M., Reynolds, R.C., 1989. *X-ray Diffraction and the Identification and Analysis of Clay Minerals*.
774 Oxford university press Oxford.

775 Morales, R.H., Murillo, M.O., Villanueva, R.A., Heredia, J.S., Zarco, F.M., 2008. Variación anual del fitoplancton
776 en el lago cráter La Alberca de Tacámbaro, Michoacán, México. *Biológicas Revista de la DES Ciencias*
777 *Biológico Agropecuarias Universidad Michoacana de San Nicolás de Hidalgo* 10, 5-17.

778 Munsell, C., 1975. *Munsell soil color charts: Munsell Color*. Baltimore, Maryland.

779 Ndayiragije, S., Delvaux, B., 2004. Selective sorption of potassium in a weathering sequence of volcanic ash soils
780 from Guadeloupe, French West Indies. *Catena* 56, 185-198.

781 Ortega-Guerrero, B., Caballero, M., Israde-Alcántara, I., 2021. The Holocene record of Alberca de Tacámbaro, a
782 tropical lake in western Mexico: evidence of orbital and millennial-scale climatic variability. *Journal of*
783 *Quaternary Science* 36, 649-663.

784 Park, J., Byrne, R., Böhnelt, H., 2019. Late Holocene climate change in Central Mexico and the decline of
785 Teotihuacan. *Annals of the American Association of Geographers* 109, 104-120.

786 Patterson, E., Swaffield, R., 1987. Thermal analysis, in: M.J., W. (Ed.), *Handbook of determinative methods in*
787 *clay mineralogy*. Blackie and Son Limited, Glasgow, UK, pp. 99-132.

788 Pedro, G., 1968. Distribution des principaux types d'altération chimique à la surface du globe. Présentation d'une
789 esquisse géographique. *Rev. Géogr. Phys. Géol. Dyn* 2, 5.

790 R Development Core Team, R., 2013. *R: A language and environment for statistical computing*.

791 Rice, S., Freund, H., Huang, W., Clouse, J., Isaacs, C., 1995. Application of Fourier transform infrared
792 spectroscopy to silica diagenesis; the opal-A to opal-CT transformation. *Journal of Sedimentary Research*
793 65, 639-647.

794 Rietveld, H., 1967. Line profiles of neutron powder-diffraction peaks for structure refinement. *Acta*
795 *Crystallographica* 22, 151-152.

796 Robert, M., Herbillon, A., 1990. Application aux argiles de sols. Genèse, nature et rôle des constituants argileux
797 dans les principaux types de sols des environnements volcaniques insulaires, *Matériaux argileux.*
798 *Structure, propriétés et applications*, pp. 539-576.

799 Saalfeld, H., Wedde, M., 1974. Refinement of the crystal structure of gibbsite, $\text{Al}(\text{OH})_3$. *Zeitschrift für*
800 *Kristallographie-Crystalline Materials* 139, 129-135.

801 Siebe, C., Guilbaud, M., Salinas, S., Chedeville-Monzo, C., 2012. Eruption of Alberca de los Espinos tuff cone
802 causes transgression of Zacapu lake ca. 25,000 yr BP in Michoacán, México, IAS 4IMC Conference,
803 Auckland, New Zeland, pp. 74-75.

804 Sigala, I., Caballero, M., Correa-Metrio, A., Lozano-García, S., Vázquez, G., Pérez, L., Zawisza, E., 2017. Basic
805 limnology of 30 continental waterbodies of the Transmexican Volcanic Belt across climatic and
806 environmental gradients. *Boletín de la Sociedad Geológica Mexicana* 69, 313-370.

807 Singer, A., 1984. The paleoclimatic interpretation of clay minerals in sediments—a review. *Earth-Science Reviews*
808 21, 251-293.

809 Smykatz, K., 1974. The determination of the degree of (dis-) order of kaolinites by means of differential thermal
810 analysis.

811 Soria-Caballero, D.C., Garduño-Monroy, V.H., Alcalá, M., Velázquez-Bucio, M.M., Grassi, L., 2019. Evidence
812 for quaternary seismic activity of the La Alberca-Teremendo fault, Morelia region, Trans-Mexican
813 Volcanic Belt. *Revista Mexicana de Ciencias Geológicas* 36, 242-258.

814 Środoń, J., 2002. Quantitative mineralogy of sedimentary rocks with emphasis on clays and with applications to
815 K-Ar dating. *Mineralogical Magazine* 66, 677-687.

816 Thiry, M., 2000. Palaeoclimatic interpretation of clay minerals in marine deposits: an outlook from the continental
817 origin. *Earth-Science Reviews* 49, 201-221.

818 Vaculikova, L., Plevova, E., Vallova, S., Koutnik, I., 2011. Characterization and differentiation of kaolinites from
819 selected Czech deposits using infrared spectroscopy and differential thermal analysis.

820 Wang, H., Li, C., Peng, Z., Zhang, S., 2011. Characterization and thermal behavior of kaolin. *Journal of Thermal*
821 *Analysis and Calorimetry* 105, 157-160.

822 Warr, L.N., 2022. Earth's clay mineral inventory and its climate interaction: A quantitative assessment. *Earth-*
823 *Science Reviews*, 104198.

- 824 Weaver, C.E., 1989. Clays, muds, and shales. Elsevier.
- 825 Winder, M., Reuter, J.E., Schladow, S.G., 2009. Lake warming favours small-sized planktonic diatom species.
826 Proceedings of the Royal Society B: Biological Sciences 276, 427-435.
- 827 Wogau, K.H., Arz, H.W., Böhnelt, H.N., Nowaczyk, N.R., Park, J., 2019. High resolution paleoclimate and
828 paleoenvironmental reconstruction in the Northern Mesoamerican Frontier for Prehistory to Historical
829 times. Quaternary Science Reviews 226, 106001.
- 830 Żarczyński, M., Wacnik, A., Tylmann, W., 2019. Tracing lake mixing and oxygenation regime using the Fe/Mn
831 ratio in varved sediments: 2000 year-long record of human-induced changes from Lake Żabińskie (NE
832 Poland). Science of the Total Environment 657, 585-596.
- 833 Ziegler, M., Jilbert, T., de Lange, G.J., Lourens, L.J., Reichert, G.J., 2008. Bromine counts from XRF scanning as
834 an estimate of the marine organic carbon content of sediment cores. Geochemistry, Geophysics,
835 Geosystems 9.

836

837 **List of figures**

838 Figure 1. (A) Regional map of North America with the location of the studied area (white
839 square), i.e. the Trans-Mexican Volcanic Belt (TMVB) in Central Mexico, and the boreal
840 summer position of the Inter-tropical Convergence Zone (ITCZ). (B) Enlarged map showing
841 the location of the three studied crater lakes Los Espinos (LLEs), Tacámbaro (LTa) and
842 Teremendo (LTe). (C) Photos of the three crater lakes (Google Earth image, 2022). (D)
843 Climatographs of the meteorological stations located nearby the three crater lakes showing
844 the monthly average temperature and precipitation data from 1981 to 2010 (Source: Servicio
845 Meteorológico Nacional, Mexico, <http://smn.cna.gob.mx/>).

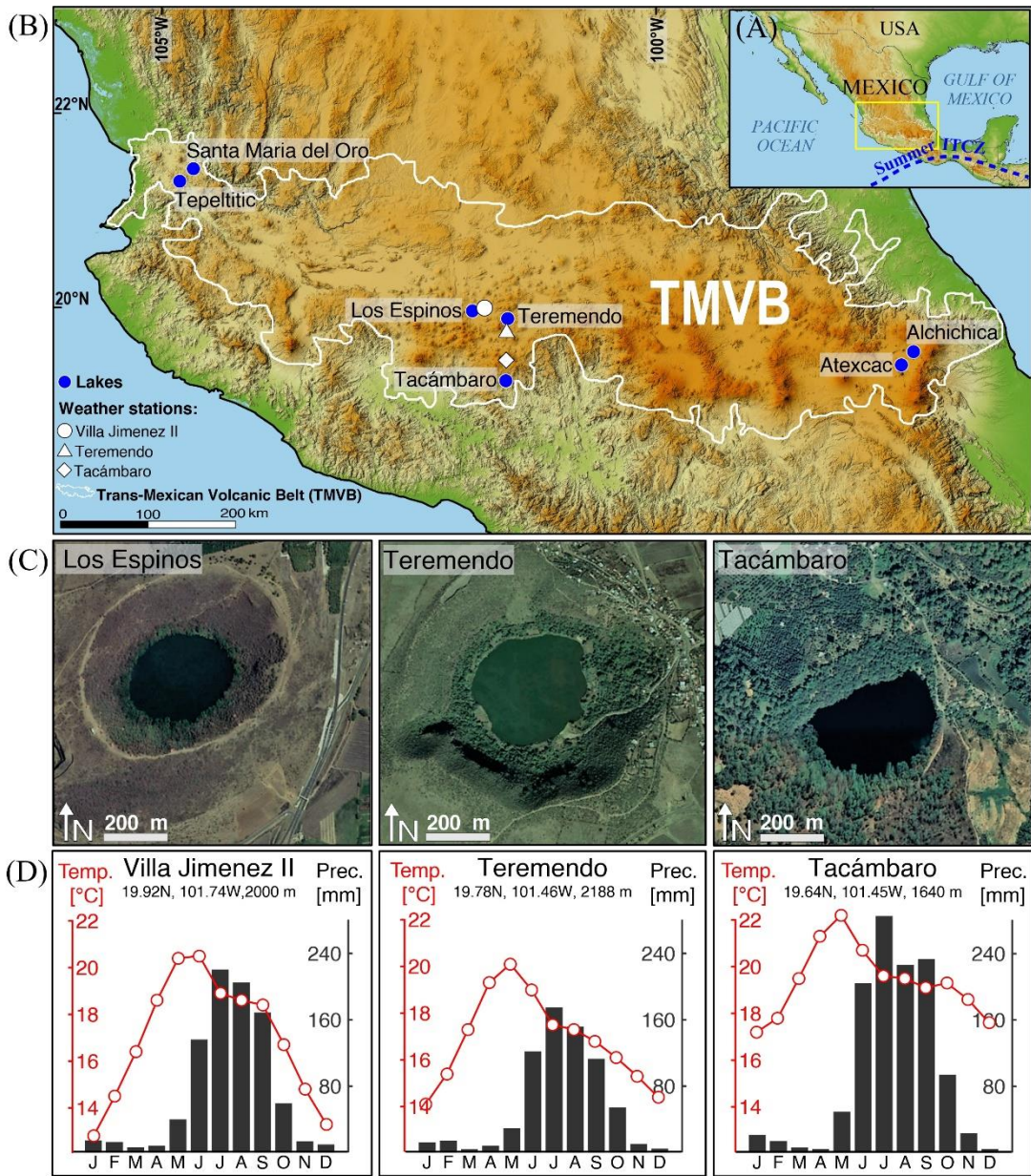
846 Figure 2. Lithology of cores LLEs19-2, LTa19-3 and LTe19-4. SCOPIX high-resolution image
847 of the core, magnetic susceptibility profiles (plain black line) and abundance of clay (% < 2
848 μm - upper axis, grey plain line) and fine silt (% 2-10 μm - lower axis, black dashed line)
849 fraction. Grain-size data are reported in Table SM1.

850 Figure 3. STA curves of sample LTA19-3 88-89 cm that contains the highest abundance of
851 kaolinite in the analyzed bulk sediments. TG, loss of weight (%): black curve, DSC: green
852 curve, DTG: blue curve.

853 Figure 4. Examples of FTIR curves on a selection of kaolinite-rich samples.

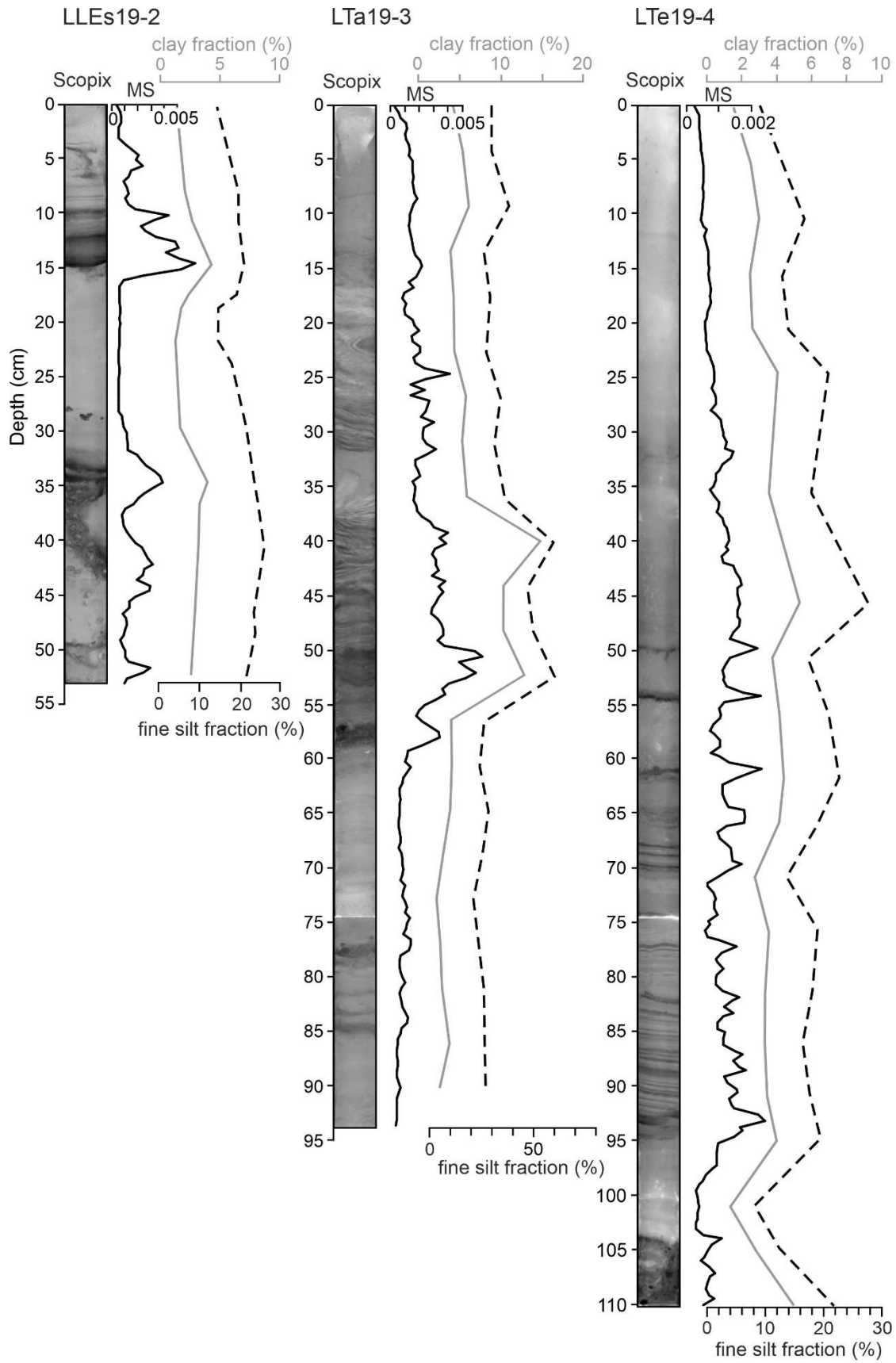
854 Figure 5. Selection of clr transformed XRF element profiles (Ti_{clr} , Br_{clr}) and elemental ratio
855 (Br/Ti) reported together with SCOPIX, PC1 score data, organic geochemistry (carbon [C]
856 and nitrogen [N] concentrations and isotope ratios), and relative clay abundance ($<2 \mu m$
857 fraction). Note the scale for SCOPIX values and clay abundance is inverted to present a
858 parallel evolution of the profiles.

859 Figure 6. Temporal evolution of relative kaolinite abundance, Ti and Br/Ti in the studied three
860 sediment cores over the past centuries. Note that the age estimates, based on $^{210}Pb_{xs}$ data, are
861 tentative beyond the past century. Comparison between temporal evolution of relative
862 kaolinite abundance, Ti and Br/Ti in core LTA19-3 and regional and local temperature and
863 precipitation trends over the past decades. Regional climate trends (indicated in colour) are
864 based on the CRU TS (Climatic Research Unit gridded Time Series) dataset (CRU TS
865 Version 4.06 - [Harris et al., 2020](#)) and local (indicated in grey) climate data derive from a
866 nearby weather station (station Tacámbaro, 16123) accessed through the CONAGUA-SMN
867 web platform (<http://clicom-mex.cicese.mx>). The annual mean for precipitation is 1168
868 mm/yr for Tacámbaro, 896 mm/yr for Villa Jimenez station (nearby lake Los Espinos) and
869 700 mm/yr for Teremendo. Thickened lines depict lowess smooth curves (span 0.1). The
870 presumed timing of the canal construction is indicated with a grey vertical bar.



871

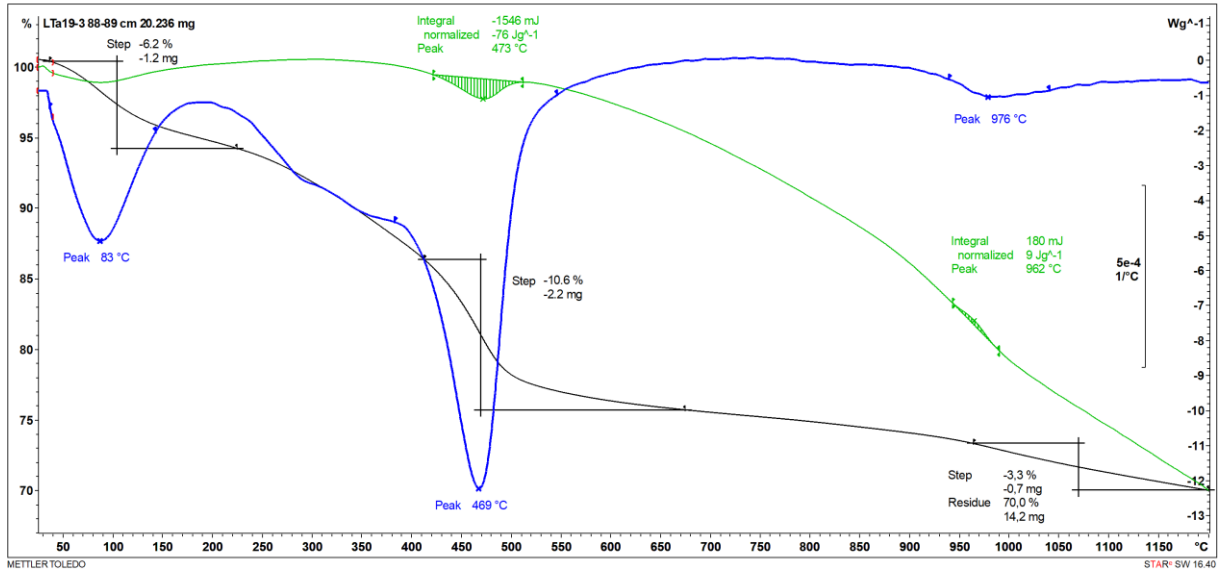
872 **Figure 1**



873

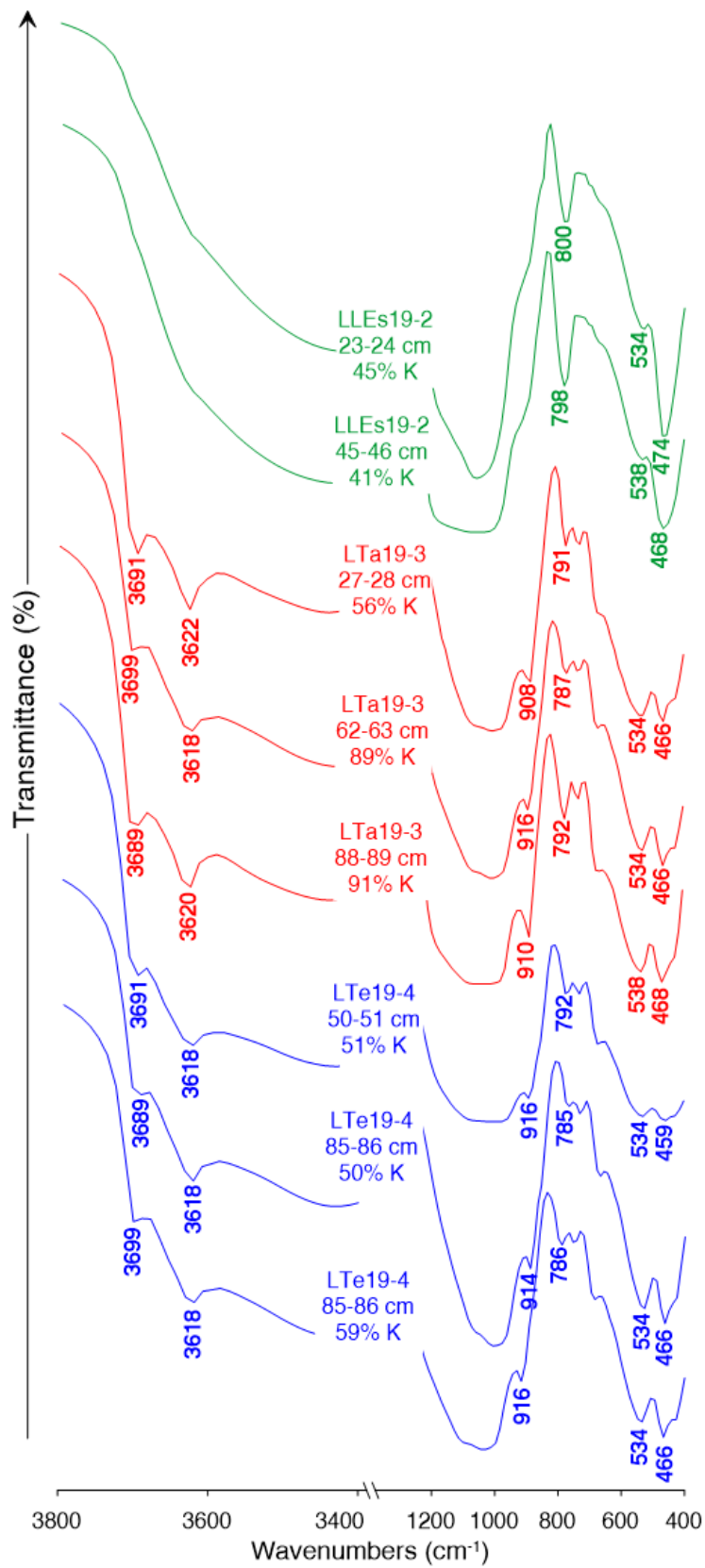
874 **Figure 2**

875



876

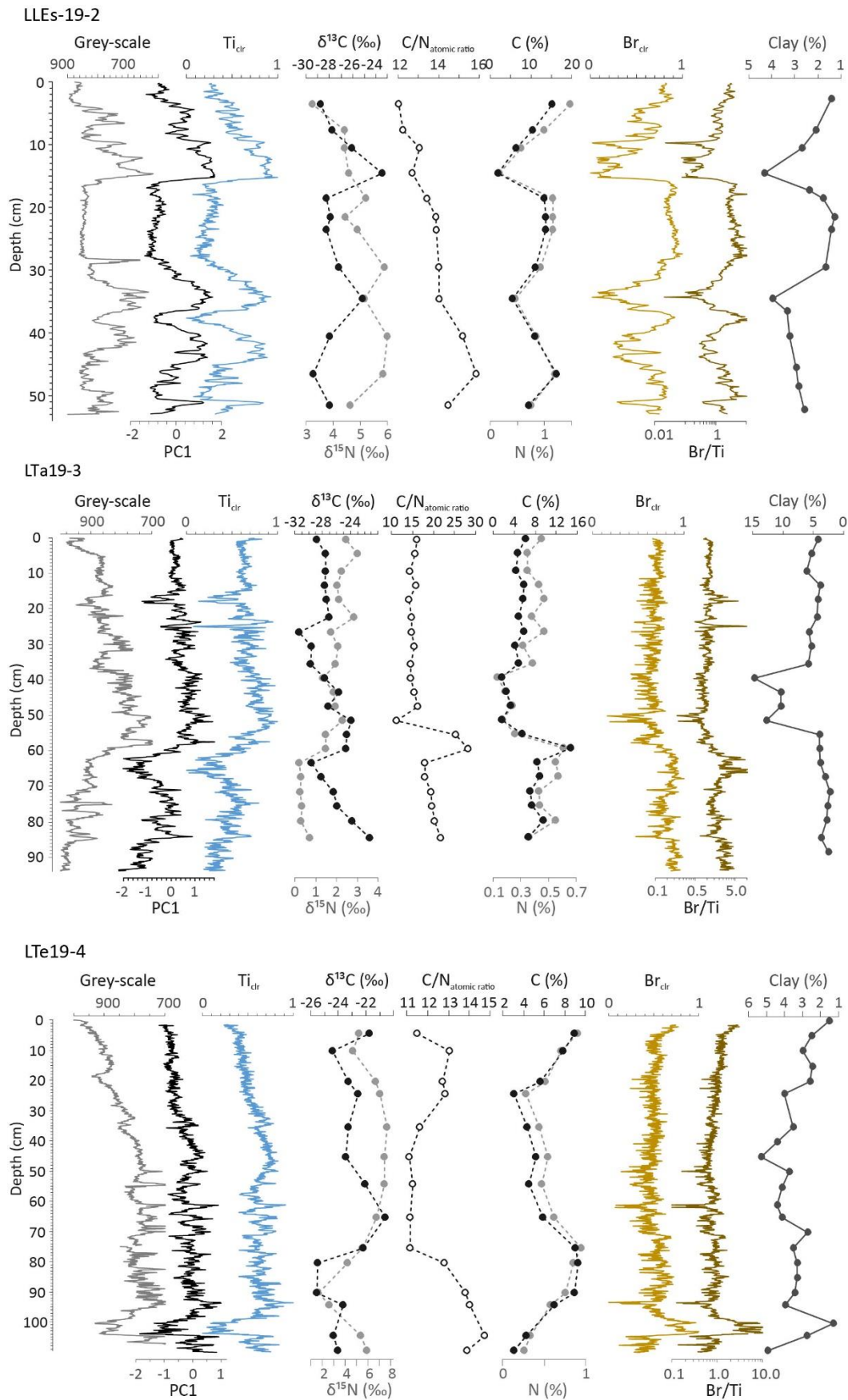
877 **Figure 3**



878

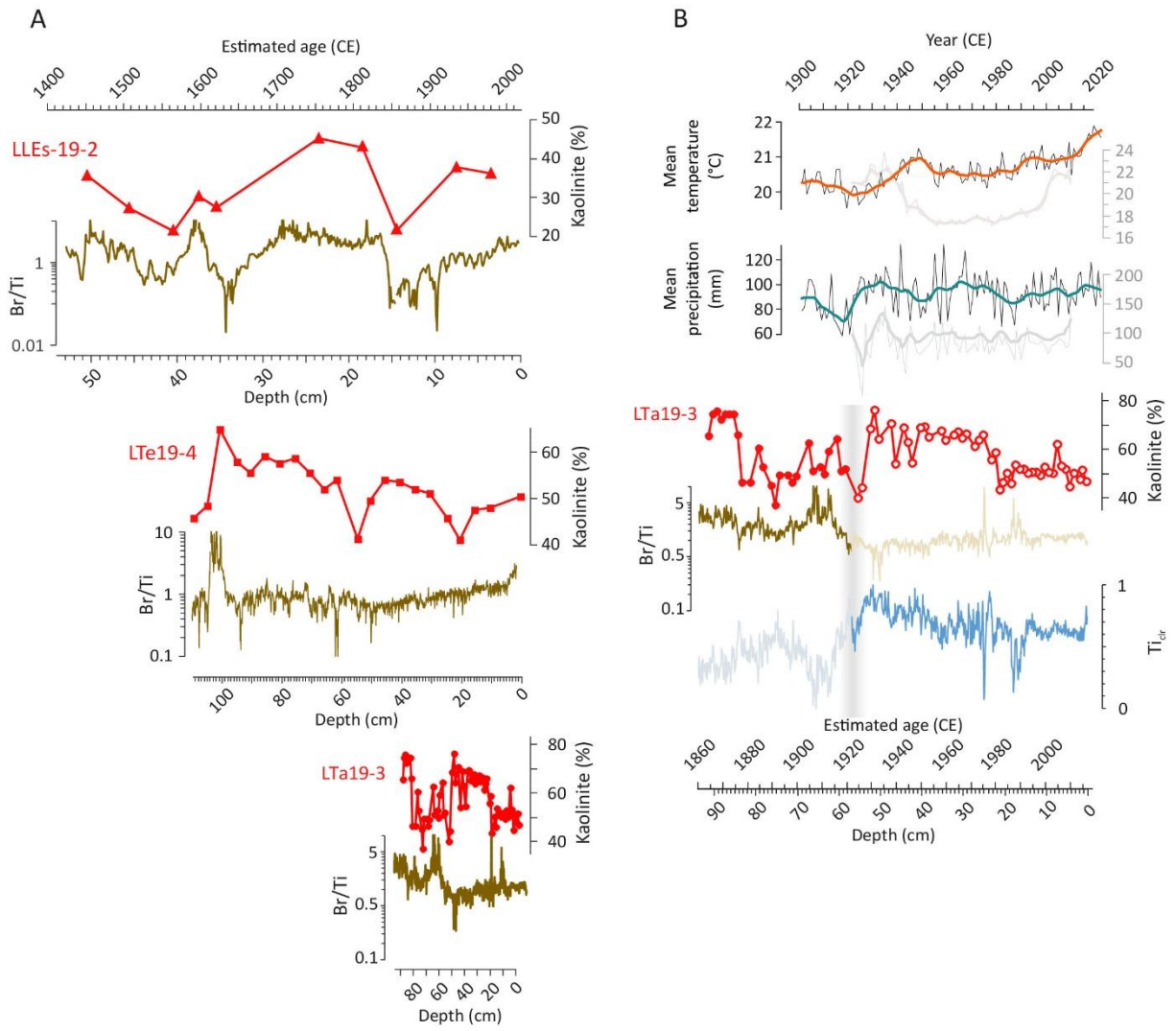
879 **Figure 4**

880



881

882 **Figure 5**



883

884 **Figure 6**